

CHAPTER 7

Nanopore-Based Optofluidic Devices for Single Molecule Sensing

GUILLAUME A. T. CHANSIN^{1,2}, JONGIN HONG^{1,2}, ANDREW J. DEMELLO¹
& JOSHUA B. EDEL^{1,2}

¹ Department of Chemistry, Imperial College London, South Kensington, London, SW7 2AZ, United Kingdom

² Institute of Biomedical Engineering, Imperial College London, South Kensington, London, SW7 2AZ, United Kingdom

7.1 INTRODUCTION

One of the primary motivations behind the development of miniaturised analysis devices has been to create new tools for modern day genomic and genetic analysis.¹ At present, much effort is directed towards designing faster and more efficient DNA analysis devices that could potentially identify the genes responsible for specific diseases.²⁻⁴ One increasingly popular approach is confinement and detection of single analyte molecules within nanofluidic structures. Such devices, have at least one dimension of the channel measuring less than a few hundred nanometres.⁵ One of the main advantages of nanofluidics is in the ability to confine single molecules within a well defined space in order to be efficiently detected. Importantly, probing molecules at the single molecule level is essential if one wants to measure fluctuations usually lost in ensemble averaged techniques.

Although there are many approaches in combining single molecule detection with nanofluidics, a promising approach over the past decade has been in the use of nanopores. In the 1990s, much effort was made to recreate and engineer nanopores outside of the living cell.⁶ Of particular interest was the α -hemolysin pore, a protein that opens a 1.5 nm-wide channel when inserted inside a lipid bilayer membrane.⁷ In 1996, Kasianowicz *et al.* demonstrated the application of α -hemolysin to measure the length of single-stranded DNA molecules.⁸ The authors could detect the blockage of the ionic current during the translocation of the molecules inside the channel. This milestone opened a new field of research through the motivation that nanopores could be used to sense and analyse nucleic acids⁹ (ibid. Chapter 6). In recent years, different approaches have been used to create nanopores with standard micro and nano-fabrication processing techniques as opposed to a biologically driven approach.^{10,11} Such devices are made using the same materials used in the semiconductor industry and thus integrate well with other top-down technologies. In this chapter, we will focus our attention on these solid-state nanopores and their potential use in fluorescence spectroscopy of single molecules.

Nanopore-based platforms are suitable for the study of single molecules as they provide a level of confinement that allows for perfect detection efficiency. This level of confinement results in an entropic barrier being overcome by the biopolymers as the molecule is unfolded when driven inside the pore. This concept can be easily explained for

macromolecules such as DNA, RNA and proteins. These molecules are long chains which can adopt a large number of conformations. They can thus be modelled using polymer physics and the size of the molecule in solution can be represented by the radius of gyration R_g . In the ideal chain approximation R_g is defined by

$$R_g^2 = \frac{1}{N} \sum_{k=1}^N \langle r_k^2 \rangle \quad (7.1)$$

where N is the total number of monomers and r_k is the distance of monomer k from the centre of mass coordinate.¹² In a more realistic model, the solvent and the excluded volumes (from interactions between monomers) must also be taken into account. In free solution, the polymer can adopt a very large number of conformations Z . Its entropy S is defined as

$$S = k_B \ln Z \quad (7.2)$$

where k_B is the Boltzmann constant.¹³ Now let us consider the polymer inside a nanopore of radius r_0 . If r_0 is much smaller than R_g the spatial confinement is such that the number of available conformation decreases (this is depicted in Figure 7.1). This decrease in entropy is called the entropic barrier and is unfavourable to the passage of the molecule inside the channel. The free energy F of the polymer is defined according to,

$$F = U - TS = U - k_B T \ln Z \quad (7.3)$$

where U is the energy of the polymer and T is the absolute temperature. At any time, the polymer tries to minimise its free energy. Hence the competing effects of external forces and entropy can induce the passage of a molecule into the channel. For example, an electric field can be used to force DNA molecules into a nanofluidic channel. This has been successfully performed and applied to the analysis of DNA stretching.¹⁴⁻¹⁶

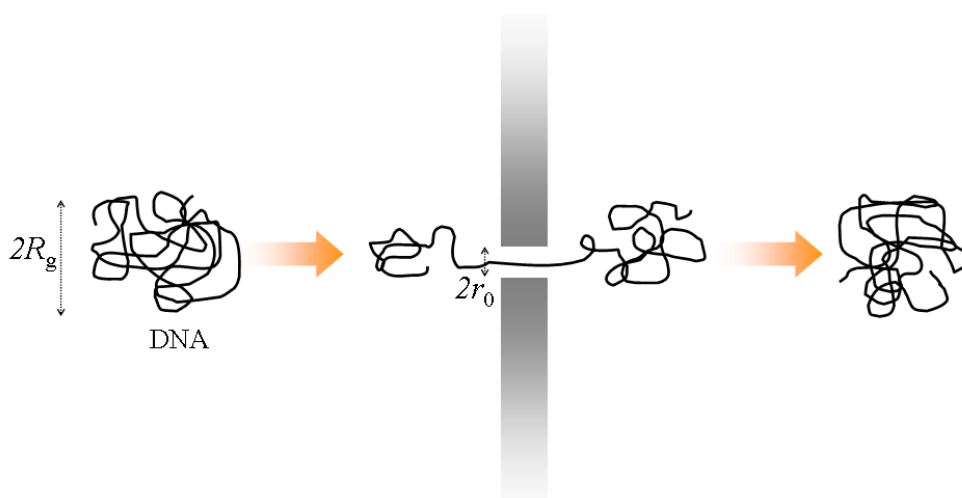


Figure 7.1 Schematic of the translocation of a DNA molecule inside a nanopore when the pore size is much smaller than the radius of gyration ($r_0 \ll R_g$).

It must be noted that the fabrication of a nanopore differs from that of a more conventional channel.¹⁰ Nanopores are generally short vertical channels in a thin free-standing membrane (Figure 7.2) offering significant advantages over planar nanofluidic devices. First, the fabrication method produces nanopores with rotational symmetry. Second, the final cross sectional geometry of the nanopore does not depend on the sealing step, with pore diameters ranging from a few 100 nm to less than 5 nm,^{17,18} depending on the drilling tool. Third, the relatively short channel length means the device is less prone to permanent clogging and decontamination is facilitated. Finally, the nanopores can be used as sub-wavelength apertures for optofluidic applications.

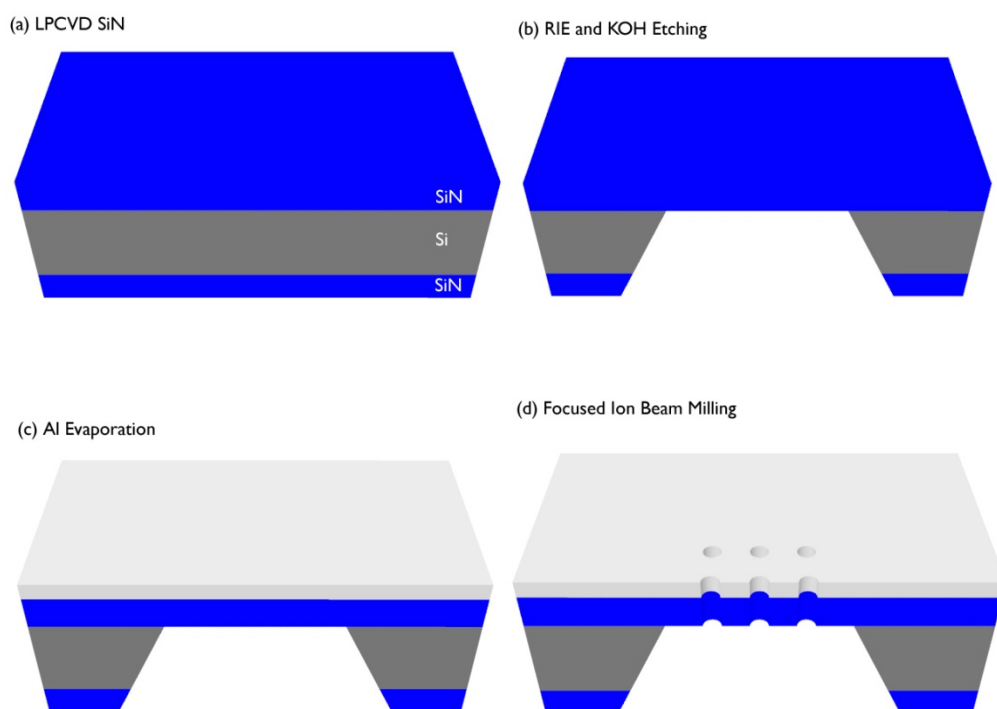


Figure 7.2 Fabrication of solid-state nanopores from a silicon wafer coated with silicon nitride (a). A window is opened in the nitride layer at the back of the wafer by standard photolithography and reactive ion etching (b). The uncovered silicon is then wet-etched with KOH to create a free standing silicon nitride membrane (b). Metal is deposited by thermal evaporation to enable the optical function of the device (c). The pores are then milled sequentially with a focused ion beam (d).

The term “optofluidic” is typically used to describe a large variety of devices that combine fluids and light.¹⁹ These include devices containing nanoholes, or nanowells in a metal film. Unlike nanopores, these devices are not made in free standing membranes, but rather are usually fabricated on top of a glass substrate. In this chapter, we will use the term nanohole to describe any device which does not incorporate a conveying fluidic channel. Although a comprehensive review of nanohole devices is beyond the scope of this chapter, they can be categorised into two different types. The first are based on surface plasmon resonance (SPR) and usually comprise an array of nanoholes in a gold or silver film. Such devices exhibit surface plasmon-mediated extraordinary optical transmission, that results from coupling between incident radiation and surface plasmon polaritons.²⁰ Any change in the refractive index due to molecular interactions in the vicinity of nanohole array will induce a shift in the transmission spectrum and thus allow both real-time and

label-free measurements to be performed.²¹ These nanohole arrays can also be used in SPR-enhanced Raman spectroscopy.²² A more detailed analysis of the underlying theory and application of this platform is provided by Sinton and co-workers in an excellent review article.²³

The second class of nanohole device exploits the sub-wavelength size of a number of holes in generating extremely small probe volumes. This feature is particularly beneficial in single-molecule fluorescence spectroscopy, allowing single molecule events to be measured in samples of relatively high analytical concentration. In the current chapter, we will describe the latter category in depth and then discuss the adaptation of this format to include nanopores in a free standing membrane.

7.2 LIGHT IN SUB-WAVELENGTH PORES

Let us consider a nanohole in a metal film. How is light transmitted through such a hole if the diameter is much smaller than its wavelength? Bethe, winner of the 1967 Nobel Prize in Physics, proposed a theoretical solution to this problem. In his 1944 paper, he considered the ideal situation of a hole in a perfectly conducting metal screen with no thickness, and found a dependence of the transmitted light on the radius-to-wavelength ratio according to,

$$T \propto \left(\frac{r_0}{\lambda} \right)^4 \quad (7.4)$$

Here T is the transmission efficiency, λ the wavelength of the incident radiation and r_0 the radius of the hole in the metal screen.^{24,25} This result shows that as r_0 is reduced below the wavelength, the transmission of light drops rapidly. Interestingly, there is no cut-off radius under which light propagation is forbidden. This implies that energy is transmitted even for very small hole radii. However, this theory is incomplete if the thickness of the metal screen is finite. In this case the ‘hole’ becomes a ‘pipe’ with metallic walls and is then better described as a circular waveguide.

7.2.1 Evanescent Fields in Waveguides

For a given wavelength λ , there are only a discrete number of propagation modes inside a waveguide due to symmetry as well as boundary conditions imposed by Maxwell’s equations. It is common to analytically solve Maxwell’s equations for two particular sets of modes: transverse-electric (TE) and transverse magnetic (TM) modes, where the direction of propagation is perpendicular to the electric field or the magnetic field, respectively. In the case of circular waveguides, these modes are written in the form TE_{pq} and TM_{pq} where p and q are integers.

Assuming r , θ , z are the cylindrical space coordinates (Figure 7.3) and t is time, each of the propagation modes has an electric field of the form (a similar equation can be written for the magnetic field)

$$\mathbf{E}_{pq}(r, \theta, z, t) = \mathbf{E}_{pq}(r, \theta) e^{i\omega t} e^{-\gamma z} \quad (7.5)$$

where the propagation constant γ is defined according to

$$\gamma = \pm \sqrt{\left(\frac{\chi'_{pq}}{r_0}\right)^2 - \omega^2 \mu \epsilon} = \alpha + i\beta \quad \text{for TE}_{pq} \quad (7.6)$$

$$\gamma = \pm \sqrt{\left(\frac{\chi_{pq}}{r_0}\right)^2 - \omega^2 \mu \epsilon} = \alpha + i\beta \quad \text{for TM}_{pq} \quad (7.7)$$

In these equations, μ and ϵ are the permeability and the permittivity of the medium filling the core of the guide, χ_{pq} is the q^{th} root of the p^{th} -order Bessel function, and χ'_{pq} is the q^{th} root of the derivative of the p^{th} -order Bessel function.²⁶

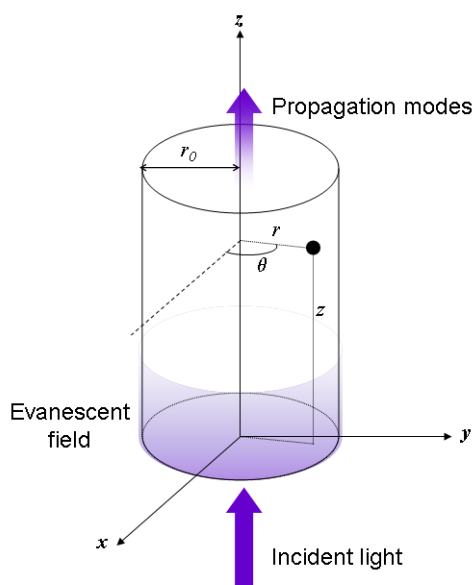


Figure 7.3 Circular waveguide in cylindrical coordinates (r, θ, z) . The cladding ($r > r_0$) is made of metal and the core ($r < r_0$) is filled with a dielectric material. Modes under cut-off condition do not propagate but generate evanescent fields at the entrance of the guide.

For small radii γ is real ($\beta = 0$) and the intensity of the field decays exponentially along the z direction (an evanescent field). A cut-off condition can be defined for $\gamma = 0$ and by inserting $\lambda = 2\pi/\omega\sqrt{\mu\epsilon}$ the cut-off diameters are given by

$$d_c = \frac{\chi'_{pq}}{\pi} \lambda \quad \text{for TE}_{pq} \quad (7.8)$$

$$d_c = \frac{\chi_{pq}}{\pi} \lambda \quad \text{for TM}_{pq} \quad (7.9)$$

For holes narrower than the cut-off diameter the mode is not allowed in the waveguide. Table 7.1 shows cut-off diameters calculated for different propagation modes. Since the wavelength depends on the refractive index of the medium inside the core of the waveguide, values are given as a percentage of λ_0 (the wavelength of the light source in

vacuum). It should be noted that TE_{11} has the smallest cut-off diameter and is called the dominant mode: if the hole is narrower than its cut-off diameter, none of the other modes will be transmitted through the waveguide (i.e. the zero-mode regime). For $\lambda_0 = 488$ nm (a wavelength commonly used in optical analyses of biological systems) the zero-mode regime is obtained for diameters below 215 nm when the core is filled with water. In most optical devices this regime is usually undesirable since there is no transmission of power or data. However the evanescent field generated at the entrance of the waveguide is of interest for optofluidic applications because this phenomenon can be exploited in high resolution fluorescence detection.

Mode	TE_{01}	TM_{01}	TE_{02}	TM_{02}	TE_{11}	TM_{11}	TE_{12}	TM_{12}	TE_{21}	TM_{21}
d_c in air	$1.22\tilde{e}_0$	$0.77\tilde{e}_0$	$2.23\tilde{e}_0$	$1.76\tilde{e}_0$	$0.59\tilde{e}_0$	$1.22\tilde{e}_0$	$1.70\tilde{e}_0$	$2.23\tilde{e}_0$	$0.97\tilde{e}_0$	$1.63\tilde{e}_0$
d_c in water	$0.92\tilde{e}_0$	$0.58\tilde{e}_0$	$1.68\tilde{e}_0$	$1.32\tilde{e}_0$	$0.44\tilde{e}_0$	$0.92\tilde{e}_0$	$1.28\tilde{e}_0$	$1.68\tilde{e}_0$	$0.73\tilde{e}_0$	$1.23\tilde{e}_0$

Table 7.1 Cut-off diameters as a percentage of the operating wavelength in vacuum. Values are dependent on the refractive index of the medium in the core of the waveguide ($n = 1$ for air, $n = 1.33$ for water).

7.2.2 Zero-Mode Waveguides

Zero-mode waveguides (ZMWs) for single molecule analysis were pioneered by Craighead and coworkers.²⁷ These devices consist of sub-wavelength holes in a metal film in the zero-mode regime, where the short penetration depth of the evanescent field is used to minimize the optical probe volume for detection. Ultra-small probe volumes are advantageous in single-molecule detection experiments since they allow interrogation of native biological samples without the need for dilution. In other words, if the detection probe volume is kept very small, instantaneous molecular occupancies will be at or below the single molecule level even for high bulk concentrations. For example, a volume of 1 fL requires that the analyte concentration is not more than 1.6 nM. In studies by Craighead's group, ZMW excitations have been performed within aluminium films as thin as 80–100 nm.^{27,28}

In the above discussion, the metal is assumed to be a perfect conductor. However, a real metal will transmit a portion of the incident electromagnetic radiation due to the inherent dispersion of the metallic dielectric function. In a typical ZMW experiment aluminium is first deposited onto a fused silica substrate and then patterned to obtain small cavities of sub-wavelength size. Fluorescence is then detected when a fluorophore reaches the bottom of the well (as is shown in Figure 7.4). Since the light is also confined by the lateral dimension of the waveguide, a detection volume of the order of attolitres to zeptolitres (10^{-18} L to 10^{-21} L) is readily achievable.²⁷ Compared to a conventional diffraction-limited confocal microscope this corresponds to a reduction in volume of two to five orders of magnitude. Such reduced volumes have been successfully exploited for single molecule detection at physiological concentrations²⁹ or for probing the surface of lipid membranes.^{28,30} Furthermore, it has been reported that molecular count rates are enhanced due to a combination of shorter fluorescence lifetimes and stronger field intensities inside the nanohole.^{31,32}

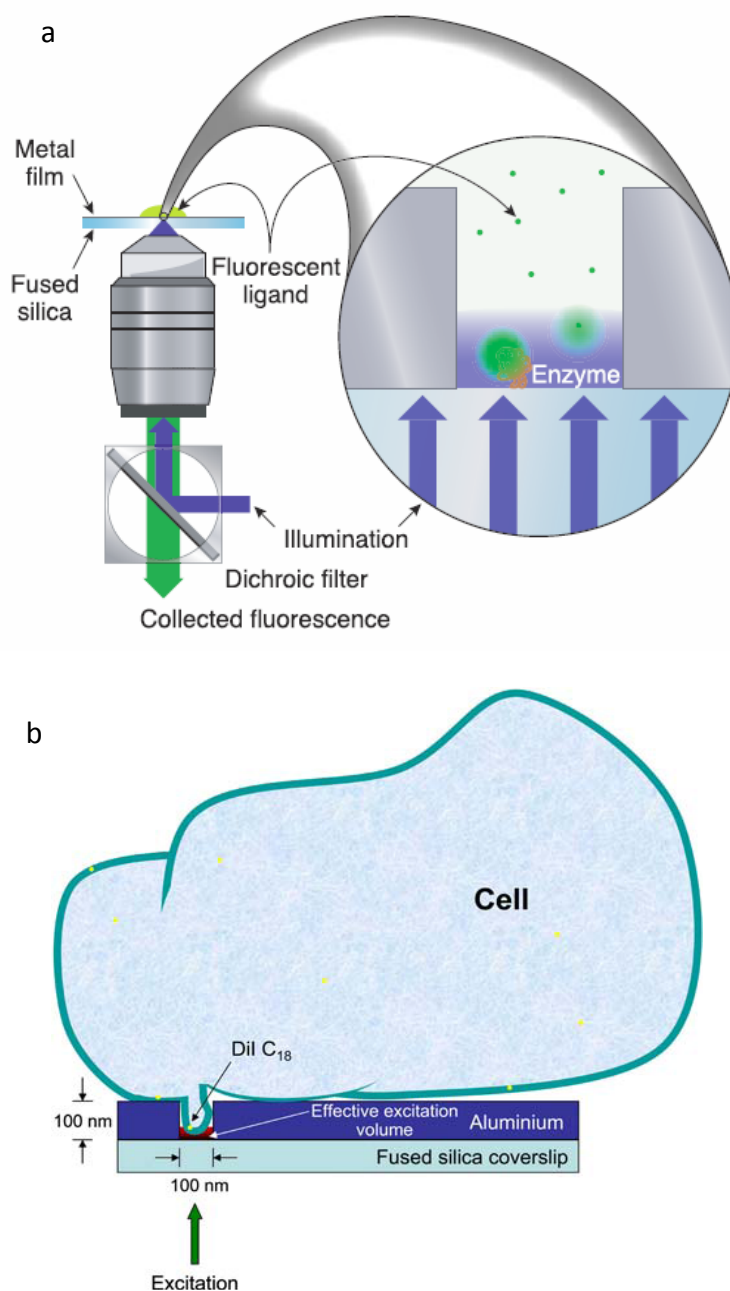


Figure 7.4 Potential applications of ZMWs. (a) Monitoring enzymatic activity. Adapted from M. J. Levene *et al.*, Science, 2003, 299, 682 and reproduced with permission. (b) Observation of single molecule along the surface of a cellular membrane. Adapted from J. B. Edel *et al.*, Biophys. J., 2005, 88, L43 and reproduced with permission.

In all experimental examples mentioned above, ZMW's have been fabricated with glass as a supporting substrate. Accordingly, analytes are not allowed to transit through the waveguide but only to diffuse in and out of the structure. However it is straightforward to notice that the geometries of a ZMW and a solid-state nanopore share certain similarities. Indeed, depending on the diameter, a cylindrical nanopore in an opaque membrane can act as a ZMW. Obtaining an optically opaque membrane is not a difficult task as several types of metal can be readily deposited on a solid-state device. The key difference when using a nanopore is the possibility of applying an external force to drive the molecules from one side of the membrane to the other. This can be done via an electrokinetic process by using

a DC voltage to induce an ionic current in solution. Under these conditions, fluorescence spectroscopy becomes a viable method for probing translocations of single molecules through a pore which acts as both a fluidic channel and an optofluidic element.

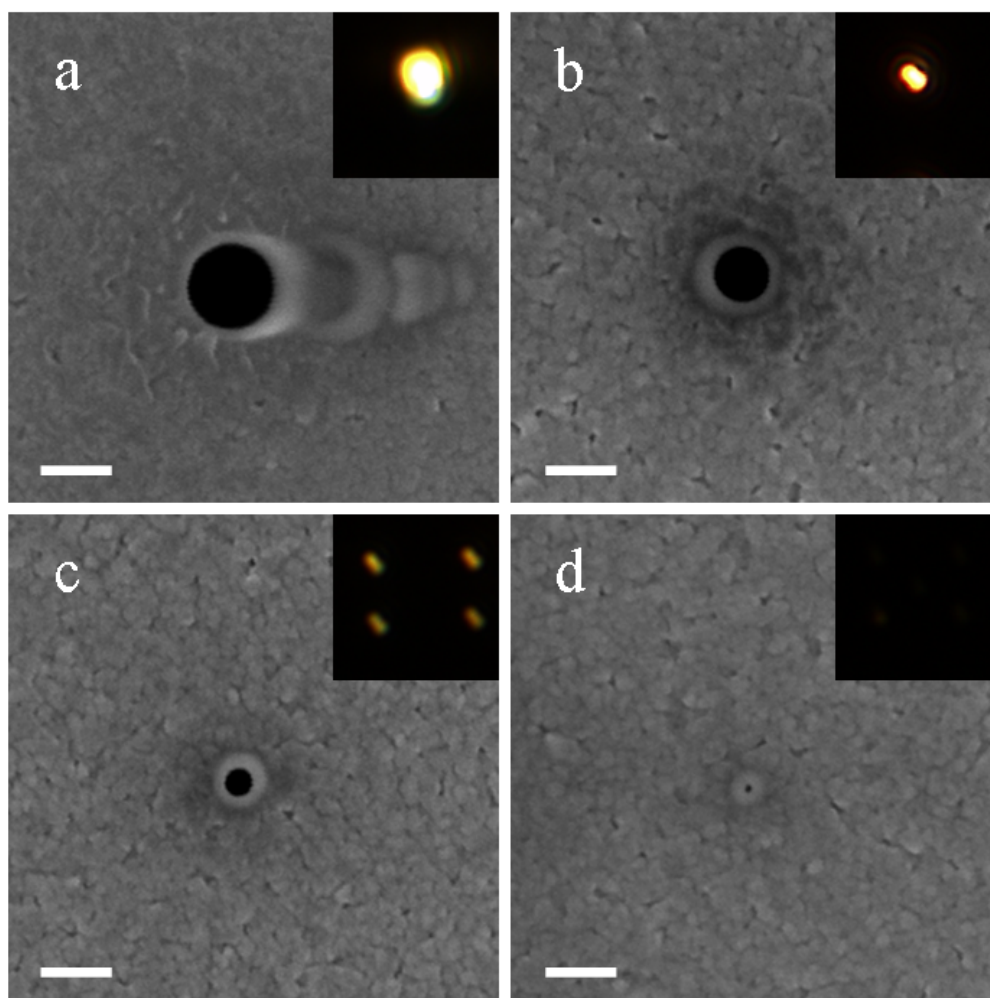


Figure 7.5 Scanning electron micrographs of nanopores in 160 nm thick membranes (60 nm SiN + 100 nm Al) with different diameters: (a) 270 nm, (b) 170 nm, (c) 100 nm, (d) 30 nm. The scale bar is 200 nm. The insets show the transmission of white light through the pores. The light is almost undetectable when the pores are 30 nm wide.

The simplest method to create a nanofluidic channel inside a solid-state membrane involves the use of focused ion beam (FIB) milling, whereby a beam of accelerated argon or gallium ions is used to remove atoms on the surface of the membrane in a physical process called sputtering. Since this method is non-selective (in terms of material preference) it can be applied to a multi-layer membrane where a metal film has been deposited on top of an initial dielectric material. Figure 7.5 shows scanning electron micrographs of FIB-milled pores of different sizes in an aluminium and silicon nitride (SiN) membrane. The integrity of the structured pores is confirmed by measuring transmitted white light using an optical microscope.

7.3 DESIGN RULES USING REAL METALS

7.3.1 Material Selection

Use of a metal layer allows suppression of light propagation through a solid-state membrane and acts as the cladding of the waveguide. As described in Figure 7.2 a thin metal film can be deposited prior to pore formation. Dielectric materials such as silicon dioxide and silicon nitride are commonly used as free-standing membranes but are optically transparent. Accordingly, it is essential that the metallic layer is thick enough to efficiently block incident light whilst not appreciably extending the nanopore length. In the waveguide theory described previously the metal cladding is considered to be a perfect conductor and the thickness of the layer has no effect on the screening efficiency. In contrast, real metals have a complex dielectric constant which can be expressed as

$$\tilde{\epsilon}_r = \epsilon' + i\epsilon'' = (n + ik)^2 \quad (7.10)$$

where n is the refractive index and k is the extinction coefficient of the material. The dielectric constant depends on the incident wavelength as do n and k . The variation of n and k as a function of wavelength is shown in Figure 7.6. Figure 7.6(b) shows that metals possess large extinction coefficients and are able to efficiently attenuate visible light.

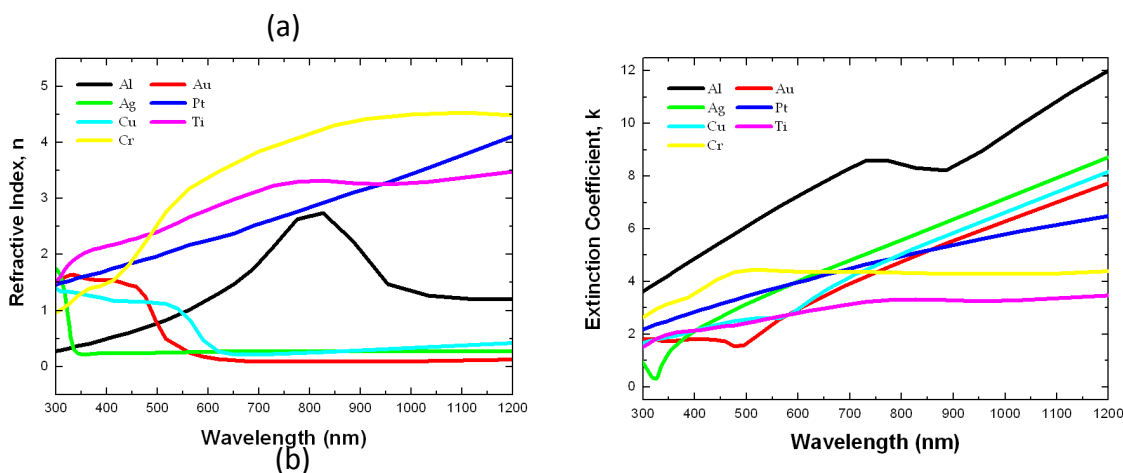


Figure 7.6 (a) Variation of refractive index as a function of wavelength and (b) variation of extinction coefficient as a function of wavelength for a selection of metals.

When detecting translocation events the signal-to-noise ratio can be maximized by ensuring that all background fluorescence from the bulk sample is removed. Accordingly, the metallic layer is crucial in efficiently screening incident light at the wavelength of interest. Two figures of merit are useful when selecting an appropriate metal for such a purpose. First, the reflectivity which is defined as the ratio of the intensity of the radiation reflected to the intensity of the incident radiation. Second, the transmission which is defined as the fraction of incident radiation that passes through the membrane. The reflectivity R at normal incidence for any absorbing media can be expressed as

$$R = \frac{(n_1 - n_2)^2 + k_2^2}{(n_1 + n_2)^2 + k_2^2} \quad (7.11)$$

where the media on each side of the interface are denoted by the numerical indices l and 2 .³³ The reflectivities of different materials illuminated at a wavelength of 488 nm are tabulated in Table 7.2. In order to evaluate the transmission through the membrane, the thicknesses of each material is fixed. Accordingly, transmittance values for different combinations of a 100 nm thick metal layer on top of a 200 nm thick dielectric layer were obtained via frequency-domain finite-element method (FEM) simulations and are listed in Table 7.3. More details on the FEM simulations performed can be found elsewhere.³⁴

Among the chosen materials, it can be observed that aluminum is the best for screening incident light, with the highest reflectivity and light attenuation properties at 488 nm. Importantly, aluminum is also free from both supporting surface plasmons (trapped electromagnetic waves at a metallic/dielectric interface formed through interaction with the free electrons in metal) and localized surface plasmons (surface plasmon modes at the edges of the hole) at 488 nm since its plasmon frequency significantly differs from the excitation wavelength. This mismatch prevents the occurrence of extraordinary transmission.

	<i>Si</i>	<i>SiN</i>	<i>SiO₂</i>	<i>Ag</i>	<i>Al</i>	<i>Au</i>	<i>Cr</i>	<i>Cu</i>	<i>Pt</i>	<i>Ti</i>
<i>n</i>	4.37	2.04	1.46	0.24	0.73	0.99	2.37	1.14	1.94	1.77
<i>k</i>	0.08	0	0	3.01	5.94	1.57	4.39	2.53	3.37	2.37
<i>Reflectivity</i>	0.28	0.044	0.0023	0.89	0.90	0.33	0.62	0.51	0.53	0.38

Table 7.2 Optical properties of different dielectric and metallic material at $\lambda_0 = 488$ nm.

	<i>No metal</i>	<i>Ag</i>	<i>Al</i>	<i>Au</i>	<i>Cr</i>	<i>Cu</i>	<i>Pt</i>	<i>Ti</i>
<i>Si</i>	-7	-35	-70	-21	-53	-31	-41	-30
<i>SiN</i>	-0.8	-31	-68	-16	-50	-27	-38	-26
<i>SiO₂</i>	-0.01	-30	-68	-15	-50	-26	-38	-25

Table 7.3 Transmittance (in dB) through membranes comprising a 200 nm thick dielectric and 100 nm thick metal layer. The values are calculated at $\lambda_0 = 488$ nm.

Specifically, for aluminum, the surface plasmon resonance is located at $\omega_s \approx \omega_p / \sqrt{2} = 10$ eV or 124 nm, where ω_s is the surface plasmon frequency and ω_p is the plasmon frequency.³⁵ Moreover, aluminum has a lower re-surface second harmonic generation radiation efficiency than all noble metals.³⁶

7.3.2 Pore Size and Probe Volume

Figure 7.7 shows electromagnetic field distributions for Al/SiN membranes containing nanopores of varying sizes at $\lambda = 488$ nm.³⁴ It can be observed that as the pore size increases, more energy is transmitted to the upper (screened) region. As has been seen previously there is no propagation for pore sizes below 215 nm (Figure 7.7(b) and (c)) and the intensity of the electromagnetic field decays evanescently along the pore-axis.

However, because the thickness of the metallic layer is much smaller than the excitation wavelength and the skin-depth in real metals (which reflects the penetration of the electromagnetic field inside the walls), the electromagnetic field inside a pore is only partially attenuated (Figure 7.7(d)). Above the cut-off diameter, an appreciable amount of the electric field is transmitted into the screened region as well as within the dielectric layer, where the electric field is strongly concentrated inside the pore (Figure 7.7(e) and (f)). Both TE_{11} and TM_{01} modes are supported in the 300 nm wide pore and the TE_{21} mode is supported in the 400 nm wide pore. In addition, guided lateral propagation within the dielectric layer can be observed.

In order to accurately time translocation events through a nanopore, the radiation should be perfectly confined and thus both the size of a nanopore (especially below the cut-off diameter) and the thickness of a metallic layer are the most important engineering parameters to control. The use of smaller pore sizes and thicker metallic layer enables enhance light confinement, however, device optimization involves the consideration of other factors such as potential pore blockage and the difficulties associated with high aspect ratio nanopore fabrication.

7.4 IMPLEMENTATION AND INSTRUMENTATION

7.4.1 Detection with a Confocal Microscope

Detection of translocations through a single nanopore can be performed using a confocal microscope. The principles of this instrument were originally developed by Marvin Minsky in 1957. Since then, confocal microscopy has been extensively exploited in fluorescence spectroscopy and single molecule detection.³⁷ Figure 7.8 shows the basic schematic of a confocal microscope that can be used in conjunction with a nanopore device. In such a setup, a laser beam is directed into the sample through a microscope objective. Emitted fluorescence photons are then collected by the same objective and sent to a detector. One of the key components of this set-up is the dichroic mirror which enables the spatial separation of the fluorescence signal from the excitation light. Essentially, an ideal dichroic mirror acts as a perfect mirror at the excitation wavelength and a transparent medium at the emission wavelength. For diffraction-limited optics, spatial resolution is dependent on the numerical aperture (NA) of the objective: the higher the NA the better the lateral optical resolution. Hence it is best to use oil or water-immersion objectives in which the NA is higher than unity. Finally, the detector must have a high quantum efficiency i.e. a high number of photoelectrons generated per incident photon. In this respect, avalanche photodiode detectors (APDs) are becoming the standard detector choice for use in low light conditions and for single molecule detection. For example, APDs operating in photon-counting mode and with a photon detection efficiency of >65% at 650 nm are commercially available.

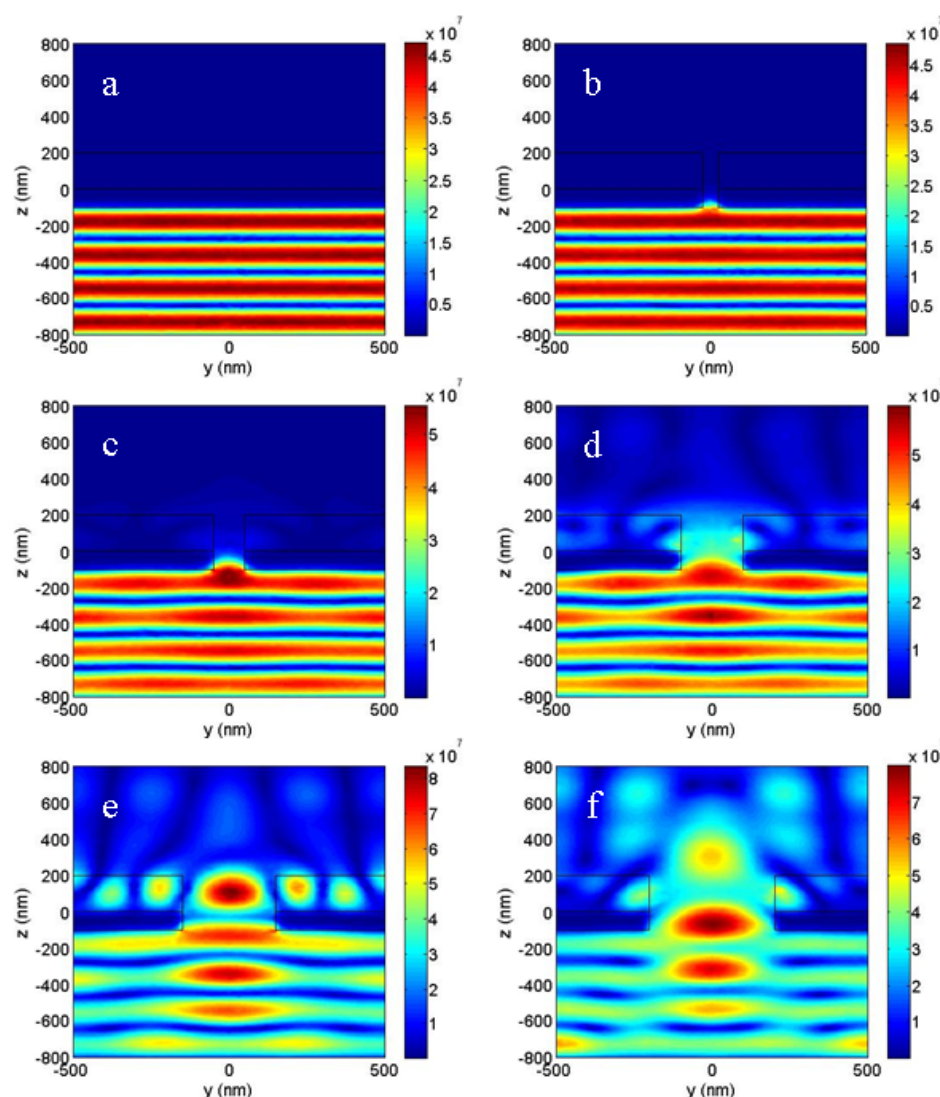


Figure 7.7 Distributions of electromagnetic field (V/m) as a function of pore diameter: (a) no hole, (b) 50 nm, (c) 100 nm, (d) 200 nm, (e) 300 nm, (f) 400 nm. Adapted from J. Hong et al., *Nanotechnology*, 2008, 19 and reproduced with permission.

By definition, a confocal microscope incorporates a small pinhole placed at the focal image plane.³⁸ The pinhole will only admit light that is focused on the aperture and rejects any out-of-focus planes. This optical sectioning provides a simple route to reducing the optical detection volume.³⁹ It should be noted that in the core experiments described herein a confocal pinhole is not an essential component, since the detection volume is already limited by the nanopores and the evanescent nature of the excitation light. However the pinhole is still useful at reducing the amount of fluorescent background during the measurement.

To initiate and observe translocations of molecules using the confocal microscope, the nanoporous membrane must be packaged so that it fulfils several requirements. First, the membrane must act as the main interface between the two reservoirs. Second, each reservoir must accommodate an electrode so that an electrophoretic force can be applied to the analyte molecules. Finally, the geometry of the bottom reservoir must be such that the distance between the membrane and the microscope objective is within focusing range.

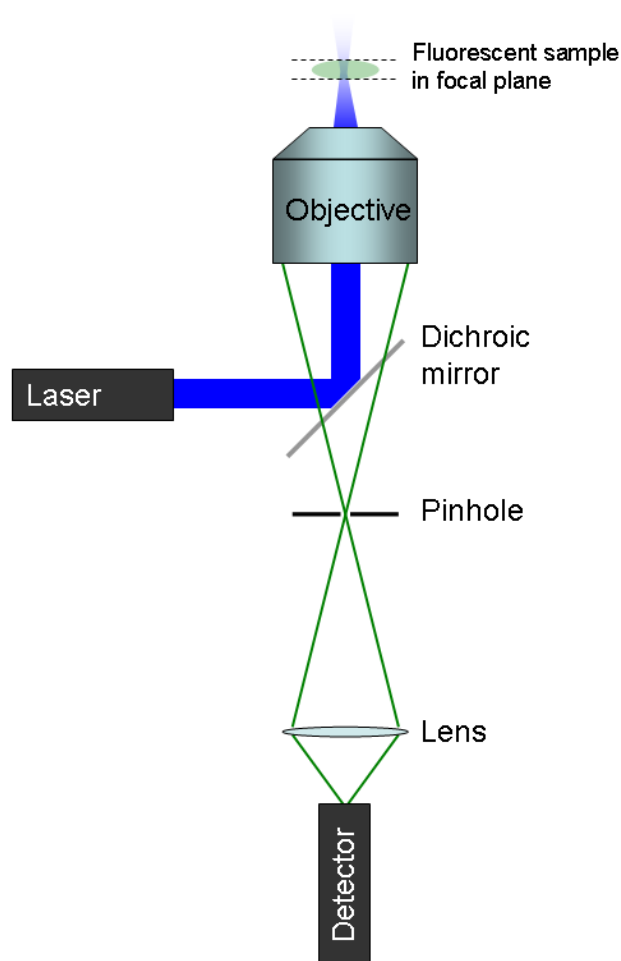


Figure 7.8 The primary features that make a confocal microscope superior to a conventional microscope are the pinhole and the objective lens. Only those rays from the best-focus point on the specimen pass through the pinhole and hit the detector. The light source is usually a laser.

Figure 7.9 depicts a schematic of the nanopore assembly where the membrane is fixed onto a glass substrate. The bottom reservoir is sealed with a glass coverslip having a thickness below 200 μm . In this situation, the coverslip is covered with a thin conductive film of indium tin oxide (ITO) on one of its surfaces. The ITO layer can then be used as the anode. A spacing layer of controllable thickness prevents any contact between the membrane and the coverslip. Figure 7.10 shows a photon burst scan of double-stranded λ -DNA (48 kbp in length) labelled with YOYO-1 as the sample. YOYO-1 is an intercalating dye and hence each DNA molecule contains more than nine thousand fluorophores along its backbone, resulting in a high signal-to-noise ratio. To generate this dataset, the laser was focused on a single pore and resulting fluorescence photons were counted using an APD. A DC voltage was applied across the membrane to drive the molecules through the pores. Accordingly, each photon burst corresponds to a DNA translocation from the top to the bottom reservoir.

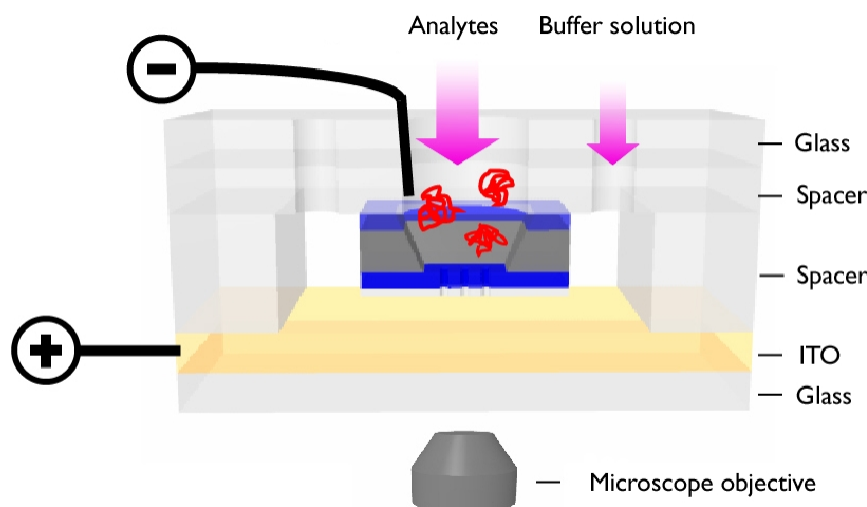


Figure 7.9 Schematic of experimental setup used to monitor DNA translocation events. Excitation light from a microscope objective is blocked by the membrane with the fluorescence signal from a translocating molecule collected by the same objective and directed to the emCCD camera. The cover slip is coated with a conductive layer of ITO. Solid-state nanopores have an average diameter of 300 nm.

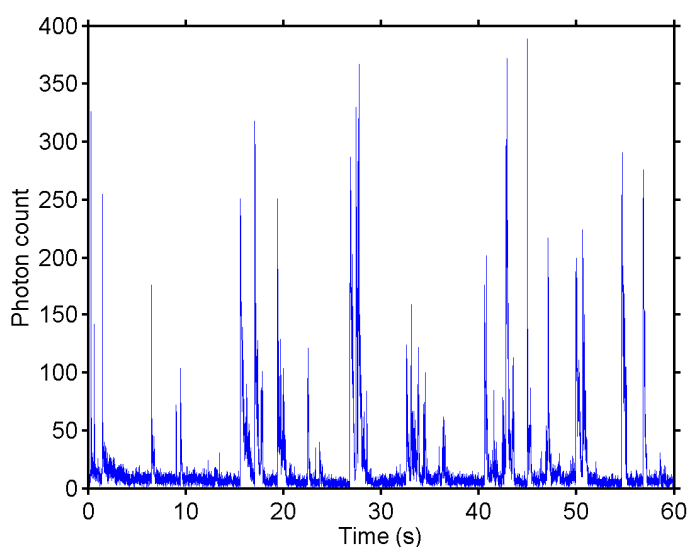


Figure 7.10 Fluorescence signal from a single pore acquired using an avalanche photodiode detector. Each peak corresponds to a single λ -DNA molecule translocating through the nanopore with a voltage of 1.60 V applied across the membrane. Data were acquired at a resolution of 50 μ s and resampled at a resolution of 5 ms. Adapted from G.A.T. Chansin et al., *Nano Letters*, 2007, 7, 2901 and reproduced with permission.

7.4.2 Probing Nanopore Arrays using a Camera

One of the advantages of solid-state membranes is the possibility of fabricating a large array of nanopores. Electrical detection of translocations in such a format is not feasible because translocation pulses from each pore will overlap. Even if molecules could be controlled in such a way that translocations occurred simultaneously, the ionic current flowing inside the pores would not provide information on individual molecules but would result from ensemble averaging instead. Conversely, an optical setup can be readily

modified to include a camera which is able to observe several pores simultaneously. It is important to note that (as with single-point detectors) the quantum efficiency of the camera must be sufficient for single-molecule detection. The frames shown in Figure 7.11 were taken with an electron-multiplying CCD (emCCD) with a quantum efficiency above 92%. The nanopores used in this experiment were 300 nm wide and are strictly speaking not ZMW.⁴⁰ However this diameter generates a stronger field intensity inside the pore, as we have seen from the simulations (Figure 7.7), and higher contrast images can be acquired.

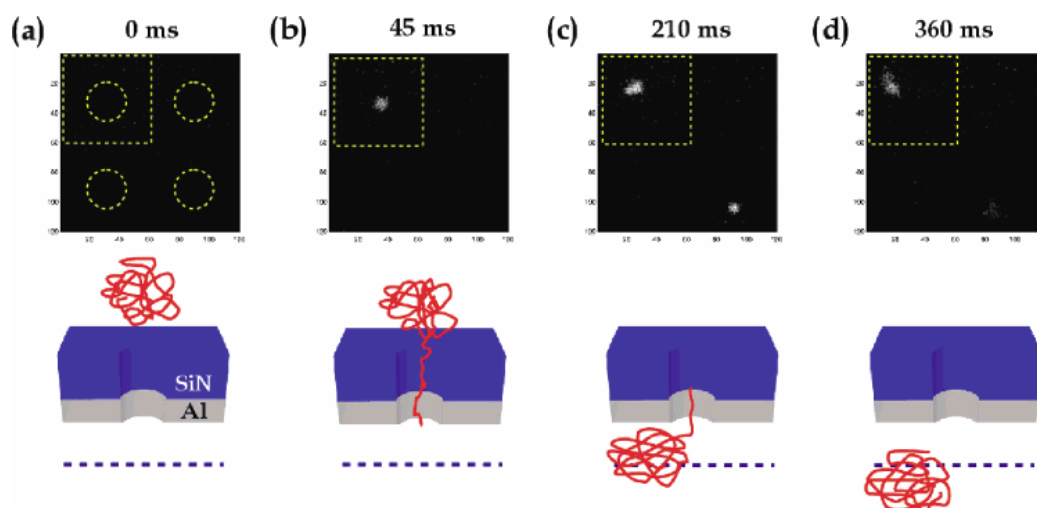


Figure 7.11 Fluorescence image of two DNA translocation events occurring under an applied voltage of 0.45 V at $t = 0$ (a), $t = 45$ ms (b), $t = 210$ ms (c), and $t = 360$ ms (d). Each pixel represents an area of 81×81 nm². The dotted circles in frame (a) indicate the location of the pores. Illustrations below each image frame provide an indication of the progression of DNA through the pore and the illumination plane (dotted line). Adapted from G.A.T. Chansin *et al.*, Nano Letters, 2007, 7, 2901 and reproduced with permission.

One of the primary issues associated with the use of a camera is the relatively low frame rate. For instance the measurements shown in Figure 7.11 were taken at a rate of one frame every 15 ms (67 Hz). In comparison the APD data were acquired at 20 kHz! Faster cameras are available but there will always be a compromise between speed and sensitivity. Moreover a higher resolution sensor will necessarily be slower because more pixels will need to be processed during readout. With these technological constraints it is important to ensure that the dwell time of the molecules in the probe volume is long enough for a signal to be acquired. Studies of the dwell time inside α -hemolysin pores have been reported previously. The velocity of single-stranded DNA during translocation is usually a constant but it has been shown that the velocity of a molecule shorter than the α -hemolysin channel is length-dependent.⁴¹ Moreover, the velocity is exponentially dependent on the applied voltage^{41,42} as well as on temperature.⁴³ Surprisingly, the velocity of double-stranded DNA in a 10 nm-wide solid state nanopore follows a very different behaviour than that of single-stranded DNA in an α -hemolysin nanopore. The duration of translocations does not grow linearly with the length of the molecule L (as expected if the velocity is constant) but scales as $L^{1.27}$.⁴⁴ From these reports it appears that, although the translocation mechanism is still not perfectly understood, voltage is the defining parameter once the molecule length, channel length and temperature have been fixed.

7.5 CONCLUSIONS

Solid-state nanopores have a great potential as tools in ultra-high throughput single-molecule analysis. Whilst most studies of nanopore systems have exploited the blockage of ionic current to observe translocations, we have seen that nanopores can also be used as optofluidic devices for high resolution fluorescence detection. Indeed by coating the solid-state membrane with an appropriate metal each nanopore can act as a waveguide where the depth and the shape of the probe volume are determined by the diameter of the pores. High-resolution confocal microscopes can be integrated with such devices to record the fluorescence signal originating from a single pore. Furthermore, unlike ionic current measurements, fluorescence can be imaged with a two-dimensional sensor, enabling the observation of a nanopore array. Probing multiple pores simultaneously has the potential to increase analytical throughput by several orders of magnitude and open paths to new applications. For example, rapid screening of a large quantity of molecules can be used for rare event detection in biological samples. Indeed, the ability to detect infrequent ($< 1:10,000$) cells in mixed cell populations is necessary for monitoring “minimal residual disease” in leukaemia and lymphoma patients and detecting small amounts of metastatic cells in solid tumour patients. There is no doubt that there is still much to explore, however nanopores appear to be a powerful new class of nanofluidic devices for measurements at the single molecule level.

References

1. G. M. Whitesides, *Nature*, 2006, **442**, 368-373.
2. A. J. deMello, *Nature*, 2006, **442**, 394-402.
3. D. Ryan, M. Rahimi, J. Lund, R. Mehta and B. A. Parviz, *Trends Biotechnol.*, 2007, **25**, 385-389.
4. J. O. Tegenfeldt, C. Prinz, H. Cao, R. L. Huang, R. H. Austin, S. Y. Chou, E. C. Cox and J. C. Sturm, *Anal. Bioanal. Chem.*, 2004, **378**, 1678-1692.
5. J. T. Mannion and H. G. Craighead, *Biopolymers*, 2007, **85**, 131-143.
6. H. Bayley, *Curr. Opin. Biotechnol.*, 1999, **10**, 94-103.
7. L. Z. Song, M. R. Hobaugh, C. Shustak, S. Cheley, H. Bayley and J. E. Gouaux, *Science*, 1996, **274**, 1859-1866.
8. J. J. Kasianowicz, E. Brandin, D. Branton and D. W. Deamer, *Proc. Natl. Acad. Sci. U. S. A.*, 1996, **93**, 13770-13773.
9. D. W. Deamer and M. Akeson, *Trends Biotechnol.*, 2000, **18**, 147-151.
10. M. Rhee and M. A. Burns, *Trends Biotechnol.*, 2007, **25**, 174-181.
11. C. Dekker, *Nat. Nanotechnol.*, 2007, **2**, 209-215.
12. M. Doi, *Introduction to polymer physics*, Oxford University Press Inc., New York, 1995.
13. M. Muthukumar, *Annu. Rev. Biophys. Biomolec. Struct.*, 2007, **36**, 435-450.
14. J. T. Mannion, C. H. Reccius, J. D. Cross and H. G. Craighead, *Biophys. J.*, 2006, **90**, 4538-4545.
15. C. H. Reccius, J. T. Mannion, J. D. Cross and H. G. Craighead, *Phys. Rev. Lett.*, 2005, **95**.
16. J. O. Tegenfeldt, C. Prinz, H. Cao, S. Chou, W. W. Reisner, R. Riehn, Y. M. Wang, E. C. Cox, J. C. Sturm, P. Silberzan and R. H. Austin, *Proc. Natl. Acad. Sci. U. S. A.*, 2004, **101**, 10979-10983.

17. C. Ho, R. Qiao, J. B. Heng, A. Chatterjee, R. J. Timp, N. R. Aluru and G. Timp, *Proc. Natl. Acad. Sci. U. S. A.*, 2005, **102**, 10445-10450.
18. A. J. Storm, J. H. Chen, X. S. Ling, H. W. Zandbergen and C. Dekker, *Nat. Mater.*, 2003, **2**, 537-540.
19. D. Psaltis, S. R. Quake and C. Yang, *Nature*, 2006, **442**, 381-386.
20. T. W. Ebbesen, H. J. Lezec, H. F. Ghaemi, T. Thio and P. A. Wolff, *Nature*, 1998, **391**, 667-669.
21. A. G. Brolo, R. Gordon, B. Leathem and K. L. Kavanagh, *Langmuir*, 2004, **20**, 4813-4815.
22. A. G. Brolo, E. Arctander, R. Gordon, B. Leathem and K. L. Kavanagh, *Nano Lett.*, 2004, **4**, 2015-2018.
23. D. Sinton, R. Gordon and A. G. Brolo, *Microfluid. Nanofluid.*, 2008, **4**, 107-116.
24. H. A. Bethe, *Physical Review*, 1944, **66**, 163.
25. C. Genet and T. W. Ebbesen, *Nature*, 2007, **445**, 39-46.
26. J. D. Kraus, *Electromagnetics*, 4th edn., McGraw-Hill, New York, 1992.
27. M. J. Levene, J. Korlach, S. W. Turner, M. Foquet, H. G. Craighead and W. W. Webb, *Science*, 2003, **299**, 682-686.
28. J. B. Edel, M. Wu, B. Baird and H. G. Craighead, *Biophys. J.*, 2005, **88**, L43-L45.
29. K. T. Samiee, M. Foquet, L. Guo, E. C. Cox and H. G. Craighead, *Biophys. J.*, 2005, **88**, 2145-2153.
30. K. T. Samiee, J. M. Moran-Mirabal, Y. K. Cheung and H. G. Craighead, *Biophys. J.*, 2006, **90**, 3288-3299.
31. H. Rigneault, J. Capoulade, J. Dintinger, J. Wenger, N. Bonod, E. Popov, T. W. Ebbesen and P. F. Lenne, *Phys. Rev. Lett.*, 2005, **95**.
32. E. Popov, M. Nevriere, J. Wenger, P. F. Lenne, H. Rigneault, P. Chaumet, N. Bonod, J. Dintinger and T. Ebbesen, *J. Opt. Soc. Am. A-Opt. Image Sci. Vis.*, 2006, **23**, 2342-2348.
33. *CRC Handbook of Chemistry and Physics*, 87th edn., Taylor and Francis, London, 2007-2008.
34. J. Hong, Y. Lee, G. A. T. Chansin, J. B. Edel and A. J. Demello, *Nanotechnology*, 2008, **19**.
35. E. Shiles, T. Sasaki, M. Inokuti and D. Y. Smith, *Phys. Rev. B*, 1980, **22**, 1612-1628.
36. D. Krause, C. W. Teplin and C. T. Rogers, *J. Appl. Phys.*, 2004, **96**, 3626-3634.
37. S. M. Nie and R. N. Zare, *Annu. Rev. Biophys. Biomolec. Struct.*, 1997, **26**, 567-596.
38. J. R. Lakowicz, *Principles of fluorescence spectroscopy*, 3rd edn., Springer, New York, 2006.
39. R. H. Webb, *Rep. Prog. Phys.*, 1996, **59**, 427-471.
40. G. A. T. Chansin, R. Mulero, J. Hong, M. J. Kim, A. J. Demello and J. B. Edel, *Nano Letters*, 2007, **7**, 2901-2906.
41. A. Meller, L. Nivon and D. Branton, *Phys. Rev. Lett.*, 2001, **86**, 3435-3438.
42. S. E. Henrickson, M. Misakian, B. Robertson and J. J. Kasianowicz, *Phys. Rev. Lett.*, 2000, **85**, 3057-3060.
43. A. Meller, L. Nivon, E. Brandin, J. Golovchenko and D. Branton, *Proc. Natl. Acad. Sci. U. S. A.*, 2000, **97**, 1079-1084.
44. A. J. Storm, C. Storm, J. H. Chen, H. Zandbergen, J. F. Joanny and C. Dekker, *Nano Lett.*, 2005, **5**, 1193-1197.

